A description of hydrometeor layer occurrence statistics derived from the first year of merged Cloudsat and CALIPSO data

Gerald G. Mace,[1] Qiuqing Zhang,[1] Mark Vaughan,[2] Roger Marchand,[3] Graeme Stephens,[4] Chip Trepte,[2] and Dave Winker[2]

[1] The occurrence statistics of hydrometeor layers covering the Earth's surface is described using the first year of millimeter radar data collected by Cloudsat merged with lidar data collected by CALIPSO (July 2006 to June 2007). These satellites are flown in a tight orbital configuration so that they probe nearly the same volumes of the atmosphere within 10–15 s of each other. This configuration combined with the capacity for millimeter radar to penetrate optically thick hydrometeor layers and the ability of the lidar to detect optically thin clouds has allowed us to characterize the vertical and horizontal structure of hydrometeor layers with unprecedented precision. We find that the global hydrometeor coverage averages 76% and demonstrates a fairly smooth annual cycle with a range of 3% peaking in October 2006 and reaching a minimum in March 2007. The geographic distribution of hydrometeor layers defined in terms of layer base, layer top, and layer thickness is described. The predominance of geometrically thin boundary layer clouds is illustrated as is the spatial distribution of upper tropospheric ice clouds in the tropics. The cooccurrence of multiple layers is shown to be a strong function of latitude and geography with cooccurring middle-level (3 km < layer base < 6 km) and high-level (base > 6 km) layers being predominant over the continents. Cloud layer overlap is also examined, and a bias due to an assumption of maximum fractional overlap in coarse resolution models is quantified and shown to be on the order of −5 to −7% globally maximizing over the high-latitude continents of the Northern Hemisphere.

1. Introduction

[2] While the horizontal distribution of hydrometeors (e.g., clouds and precipitation) has been observed from the surface [e.g., *Warren et al.*, 1988] and from space [e.g., *Rossow and Schiffer*, 1999], the vertical distribution and internal structure of hydrometeor layers has remained largely unobserved on global scales. This lack of knowledge has resulted in general circulation models (GCM) agreeing reasonably well with top of atmosphere (TOA) radiative constraints yet disagreeing substantially on the manner in which that energetic balance is achieved within the simulated climate system [*Zhang et al.*, 2005]. These disparities are due to multiple compensating errors that also result in large differences in the feedbacks between the hydrological cycle and the climate system [*Soden and Held*, 2006; *Potter and Cess*, 2004]. Focusing on these differences in GCMs through creation of dynamic composites, *Bony et al.* [2006] found that many cloud regimes are poorly simulated by all climate models and that the differences in global feedback processes largely result from these poorly simulated cloud regimes. This point was expanded upon by *Williams and Tselioudis* [2007], who show that the differences among models of the global cloud response under a changing climate are due primarily to poor representations of the distributions of cloud regimes in the present climate.

[3] Our ability to document the occurrence and vertical structure of hydrometeor layers in the atmosphere has advanced substantially with the launch of two active remote sensing satellites in late April 2006. The NASA-sponsored Cloudsat and CALIPSO satellites carrying the millimeter wavelength cloud profiling radar (CPR) [*Im et al.*, 2005] and the cloud-aerosol lidar with orthogonal polarization (CALIOP) [*Winker et al.*, 2007; 2003], respectively. As discussed below, these two satellites are maintained in tight orbital coordination so that they image the same volumes of the atmosphere within 15 s of one another. Cloudsat and CALIPSO are also components of the A-Train satellite

[1]Department of Meteorology, University of Utah, Salt Lake City, Utah, USA.
[2]NASA Langley Research Center, Hampton, Virginia, USA.
[3]Joint Institute for the Study of the Atmosphere and Ocean, University of Washington, Seattle, Washington, USA.
[4]Department of Atmospheric Science, Colorado State University, Fort Collins, Colorado, USA.

constellation [*Stephens et al.*, 2002] composed of the NASA Aqua and Aura multiinstrument satellites, and the French satellite PARASOL. The synergy of the A-Train approach to Earth observation has the potential to advance our understanding of atmospheric hydrological processes.

[4] It has long been understood that a thorough characterization of the hydrometeor distribution profile requires measurements from both lidar and millimeter-wavelength radar [*Sassen*, 2002]. Radar reflectivity is proportional to the sixth moment of the particle size distribution when the particles are small with respect to the wavelength. The small Rayleigh scattering cross section and weak absorption of most cloud volumes allows the radar pulse to penetrate deep within cloud layers such that significant attenuation of the pulse to the extent that cloud boundaries are obscured typically occurs only in moderately heavy rain [*Haynes and Stephens*, 2007]. Cloud particles are generally large with respect to the lidar wavelength, and the lidar can be shown to be sensitive to the cross-sectional area or second moment of the particle size distribution. The concentrated energy within the laser pulse and the vastly larger scattering cross section at visible wavelengths relative to that in the millimeter spectrum enables lidar to detect the scattering from very tenuous clouds and aerosol layers. These properties also ensure, however, that the lidar pulse suffers significant attenuation beyond a visible optical depth of about 3 from the layer top. Merging the capabilities of radar and lidar allows us to effectively observe the majority of hydrometeor layers within the Earth's atmosphere. The most difficult scenario for the combination of Cloudsat radar and CALIPSO lidar occurs when low-level water clouds (most notably non-drizzling cumulus or stratocumulus) occur beneath higher-level clouds with optical depths that fully attenuate the lidar pulse.

[5] In this paper we attempt to contribute to an understanding of the hydrological processes in the Earth's atmosphere by presenting an initial examination of the global distribution of hydrometeor layers as resolved by merging the Cloudsat geometrical profiling product (GEOPROF) [*Mace et al.*, 2007; *Marchand et al.*, 2008] and the CALIPSO Vertical Feature Mask (VFM) [*Vaughan et al.*, 2004]. This combined data set is referred to as the Radar-Lidar Geometrical Profile Product (RL-GEOPROF); the RL-GEOPROF data set has been released publicly and can be acquired at the Cloudsat data processing center at http://www.Cloudsat.cira. colostate.edu/. Because the polar regions present a unique set of issues, for the purpose of brevity, we consider these quantities equatorward of about 70° in each hemisphere in the present paper. In this initial study, we also do not compare day and night, land and ocean, or seasonal statistics but defer those analyses to later papers.

2. Data Description and Data Stream Merging Approach

[6] The Cloudsat and CALIPSO satellites are maintained in their nominal 705 km orbit within very stringent spatio-temporal tolerances to facilitate the merging of the respective data streams. In general, the Cloudsat and CALIPSO ground tracks are oriented approximately 215 km east of the Aqua ground track at the equator on the ascending node in order to keep the CALIPSO footprint out of the sun glint region seen by Moderate Resolution Interferometer Spec-

trometer (MODIS). This displacement maximizes the comparison opportunities of aerosol properties retrieved using CALIPSO and MODIS data. Cloudsat passes over the MODIS Aqua cross track swath on average about 1 min after the MODIS measurements are made and CALIPSO is, on average, 15 s behind Cloudsat. CALIPSO and Cloudsat during the period of study pointed 0.3° and 0.16° from nadir and along the ground tracks, respectively.

[7] The footprint sizes and the vertical resolutions of the two instruments are quite different from one another, and we attempt to exploit this difference in merging the two data streams. The instantaneous footprint of Cloudsat is a circle of 1.4 km diameter. With a pulse repetition frequency of 4.3 kHz and a 0.16 s integration period, 688 pulses are averaged creating an effective footprint dimension of approximately 2 km along track. A 3.2 ms pulse is used resulting in an instantaneous resolution volume of 480 m, and the data are oversampled once to create range bins separated by 240 m. The 20 ns laser pulses from CALIOP illuminate a 70 m diameter circle on the ground and the backscattered pulse is sampled with a range resolution of 15 m. Below 8.2 km altitude, each 532 nm profile is averaged on board to 30 m vertical resolution [*Winker et al.*, 2007]. Center-to-center spacing of individual CALIOP profiles is 333 m. Above 8.2 km, the CALIOP data are further averaged horizontally to create a 1 km along-track resolution and in the vertical to create a 60 m resolution. The CALIOP version 1 data are used in this study while the Cloudsat data version is referred to as R04.

[8] There was a goal prior to launch to manage the Cloudsat and CALIPSO orbital tracks so that that at least 50% of the CALIOP profiles would reside within a CPR footprint. Given a cross track dimension of the Cloudsat footprint of 1.4 km and the fact that Cloudsat points just slightly off nadir along the orbital track, a difference between the CALIOP ground track and the CPR footprint of more than 700 m would mean that the data are not spatially coincident. Analyses of the first 14 months of data suggest that coordination of the satellite pointing is much better than planned. Separation distances of the Cloudsat and CALIPSO ground tracks are less than 700 m more than 90% of the time (T. Boain, personal communication, 2007). We can be reasonably confident, therefore, that the CALIOP data are collected from sample volumes that lie within the sample volumes of Cloudsat with a slight time offset.

[9] As described by *Mace et al.* [2007], each CPR sample volume is evaluated for the presence of hydrometeors using a hydrometeor mask algorithm described by *Marchand et al.* [2008]. The radar cloud mask, the radar reflectivity, the MODIS cloud mask [*Ackerman et al.*, 1998], and the 240 m MODIS cloud fraction within the 15 surrounding 1 km MODIS pixels are stored in what is called the Geometrical Profile product (publicly available as the level 2 GEOPROF product). Because many cloudy volumes have a reflectivity near or below the detection threshold of the CPR, the radar cloud mask is not a simple binary variable but includes confidence levels as to the degree of certainty that a given resolution volume contains a return signal that is different from instrument noise. *Marchand et al.* [2008] describes this topic in detail. In constructing a combined radar-lidar cloud mask we have chosen a radar mask threshold of 20, which is estimated to have a false positive indication of 5%.

[10] Within a CPR sample volume, CALIOP sample volumes are collected from coincident lidar pulses that lie
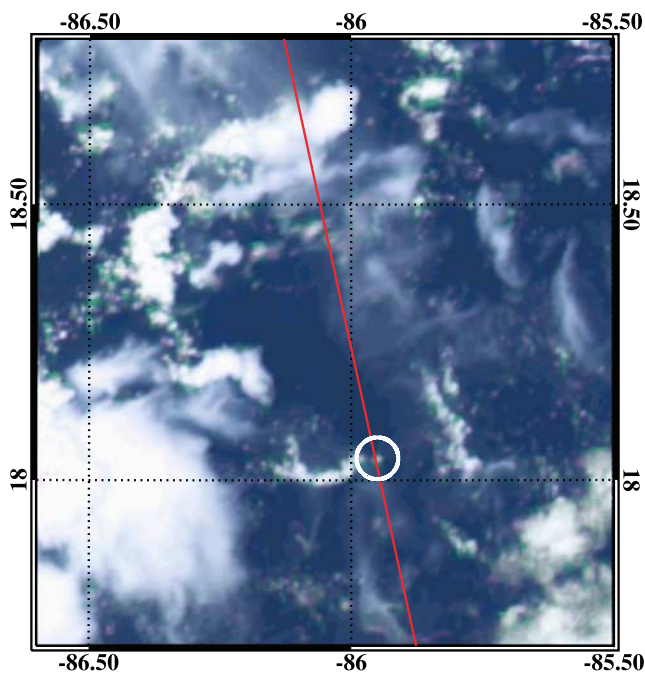
Figure 1. Aqua MODIS imagery created from 500 m resolution visible channels. Data were collected on 30 July 2006 east of the Yucatan Peninsula. The red curve extending through the image marks the path of the Cloudsat and CALIPSO satellites and the ER2. The white circle near 18.05°N latitude denotes a region illustrated in more detail.

within the radar footprint both vertically and horizontally. Lidar profiles are evaluated for the presence of clouds and/ or aerosols with an adaptive thresholding algorithm that is applied to successive iterations of a multiscale spatial averaging routine. Among the several outputs derived from this analysis is a vertical feature mask (VFM) data product, which provides a concise characterization of the cloud content and type for each range-resolved volume sampled by the lidar [*Vaughan et al.*, 2004]. The VFM is available from the Atmospheric Science Data Center at NASA Langley. The RL-GEOPROF product then consists of a CPR range bin by CPR profile array that records the fraction of the total number of lidar sample volumes (both horizontally and vertically) within a CPR sample volume reporting lidar backscatter from clouds (we hereafter refer to this quantity as Lfrac for convenience). Within RL-GEOPROF, we also report the bases and tops above mean sea level of hydrometeor layers and provide information as to which instrument observed each layer boundary. To be classified as an additional layer, we require that at least 4 hydrometeor-free range bins (960 m) exist between range bins with hydrometeors. A radar-lidar cloud mask can be created simply by evaluating the layer base and top variables in RL-GEOPROF. A more detailed cloud mask can also be created by combining the Lfrac array with the CPR cloud mask from the GEOPROF product. In the following analysis, we define a CPR volume as containing hydrometeors when LFrac $\geq$ 0.5 or the radar cloud mask has a value greater than 20.

[11] In Figures 1−4, we illustrate the procedure described above using measurements collected during the Cloudsat-CALIPSO Validation Experiment (CCVEX) that took place from Warner-Robbins Air Force Base during July and August 2006. During this campaign, the Cloud Radar System (CRS) [*Li et al.*, 2004] and the Cloud Profiling Lidar (CPL) [*McGill et al.*, 2004] collected data from the NASA ER2 during several coordinated flights along the Cloudsat-CALIPSO track. The case study illustrated in Figures 1−3 was collected on 30 July 2006 east of the Yucatan Peninsula along the track shown in Figure 1. The lidars are able to resolve the very thin cirrus layer just below 15 km (Figure 2) as well as the thicker cirrus between 12 and 13 km. The radars are also able to sense much of the lower more optically opaque cirrus nearer the convection while much of the more tenuous cirrus has a reflectivity below the CPR detection threshold of −32 dBZe. The radars are able to penetrate through much of the deep convective system near 18.65°N. Incidentally, the vertical stripe of high reflectivity near 18.3°N in Figure 2a is due to the CPR illuminating the ER2 as Cloudsat passed over the aircraft.

[12] The graphics depict excellent agreement in cloud structure resolved by the airborne remote sensors and the space-based instruments. Subtle differences due to the geometries of the fields of view can be noted, especially between the CRS and Cloudsat where the footprint and vertical resolution size differences are most extreme. Cloudsat is slightly more sensitive than CRS at the time of this flight although good agreement can be seen in the radar reflectivities. Good agreement as well is noted in the lidar attenuated backscatter measurements reported by the CPL and CALIOP. An analysis of the calibration of the Cloudsat CPR is presently underway and will be reported on separately (S. Tanelli, private communication, 2007).

[13] The results of merging the Cloudsat and CALIPSO data are shown in Figures 2e and 2f. With the exception of the boundary layer clouds near 18.05°N, LFrac is nearly 1 everywhere except along the horizontal and vertical edges of the cloud features and in the thin cirrus layer near 18.5°N. The LFrac variable (Figure 3, bottom) shows that at the Cloudsat horizontal and vertical resolution, most of the volumes were only partially filled by the shallow boundary layer clouds. Figure 3 shows an individual CPR resolution volume taken from the profile marked by an arrow in Figure 3. The CALIOP profiles that fall within the area that approximates the CPR footprints in Figure 3 (top) are evaluated in Figure 3 (bottom). In this case, the small cumulus element did not fill the CPR resolution volume entirely in the vertical dimension. The RL-GEOPROF analysis of the Cloudsat-CALIPSO track along the cumulus cloud field shown in Figure 4 also provides LFrac values that are less than 0.5.

[14] Several issues regarding the merged data set must be kept in mind. Inspection of the VFM suggests that layers are correctly identified as cloud or aerosol much more than 90% of the time. However, the product has not yet been formally validated. The CALIPSO cloud-aerosol discrimination (CAD) algorithm relies on two sets of empirically derived, multidimensional probability distribution functions (PDFs) that separately characterize the altitude-dependent backscatter intensities and spectral dependences of both clouds and aerosols [*Liu et al.*, 2004]. Misclassifications can occur whenever these PDFs overlap; that is, in those regions of space where the probabilities for both clouds and aerosols are simultaneously nonzero. This situation occurs most commonly for dense aerosol layers, which can often be mislabeled as
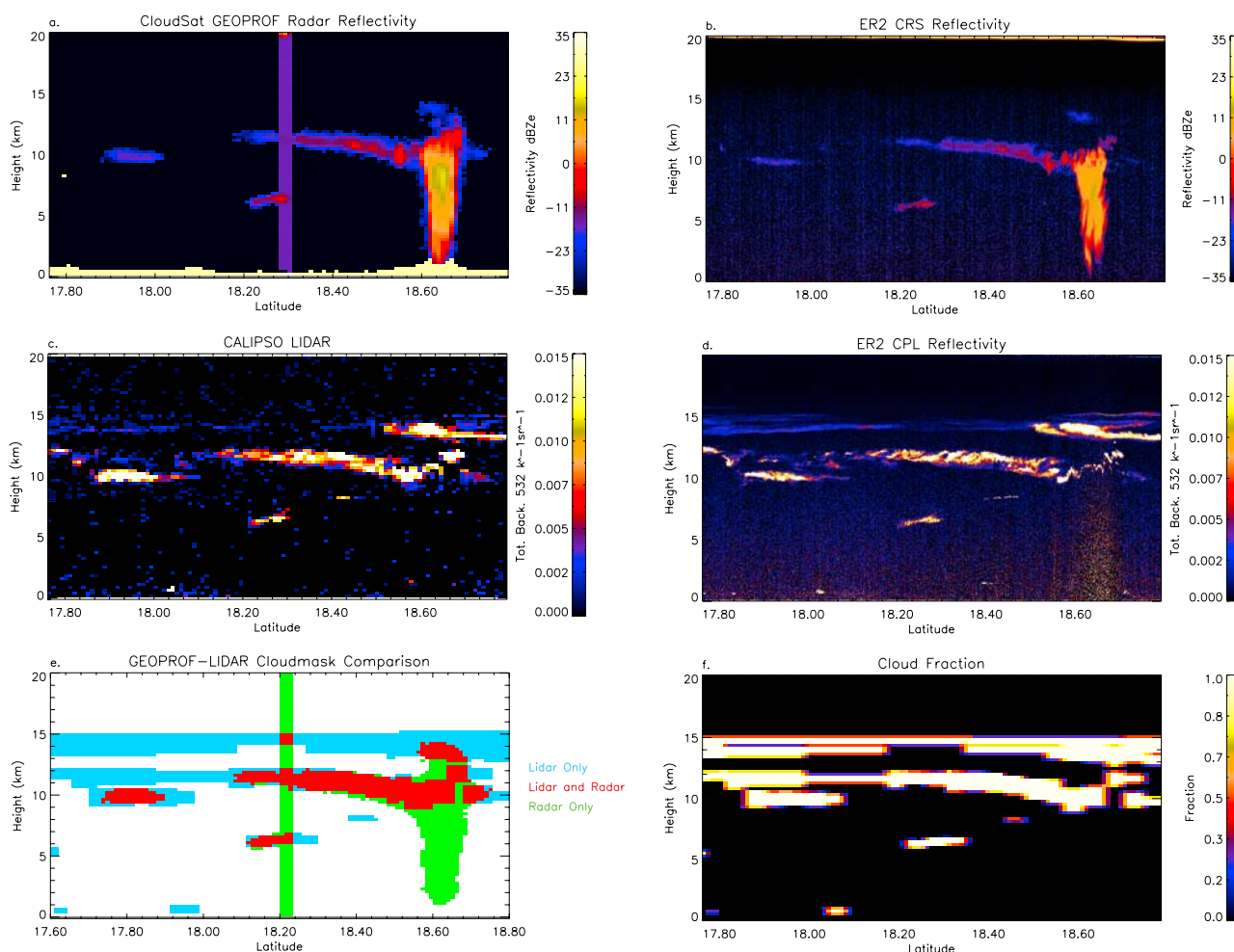
Figure 2. Radar and lidar data collected along the track depicted in Figure 1. (a) Radar Reflectivity Factor (dBZe) from the CPR on Cloudsat. (b) As in Figure 2a, except data collected by the CRS on the ER2. (c) 532 nm attenuated backscatter data collected by the CALIOP on CALIPSO. (d) As in Figure 2c, except data collected by the CPL on the ER2. (e) Mask depicting identified hydrometeor boundaries in terms of the observing instruments. (f) The Lfrac array depicting the fraction of CALIOP volumes within the CPR volumes that observed cloud.

cloud. The algorithm can identify clouds embedded within aerosol layers but because the algorithm treats each profile independently, small regions within an aerosol layer can be misidentified as cloud. Clouds located at the top of aerosol layers may cause the aerosol under the cloud to also be classified as cloud. Actual clouds occurring within aerosol layers appear to be correctly classified as cloud most of the time. Additionally, portions of the bases of some cirrus clouds are mislabeled as aerosol. In the polar regions, there appear to be some systematic misclassifications. We have noticed that in Antarctic winter, clouds near the surface are classified as aerosol while polar stratospheric clouds are classified as clouds in the data set and no effort is presently made to identify them in RL-GEOPROF. In the Arctic, boundary layer aerosols are consistently classified as cloud in certain conditions. We emphasize that these issues appear to be minor and do not significantly influence the overall results of the present analysis.

[15] In the results that we describe below, we combine the day and night data and do not attempt to evaluate differences between them. While in some circumstances, diurnal

variability is known to occur such as in the subtropical boundary layer stratocumulus regimes, we do find differences in sensitivity between the day and night VFM data in the upper troposphere that suggest that differences in detection thresholds due to background solar noise are resulting in more thin clouds being identified at night.

[16] It should also be noted that in this paper we make no attempt to distinguish between clouds and precipitation as these would normally be defined. Therefore, we refer to layers that return significant backscattered power to the radar or are deemed to be nonaerosol by the VFM as a hydrometeor layer. *Haynes et al.* [2009] find that approximately 11% of all columns with identifiable hydrometeors in the atmosphere are precipitating at a rate greater than 3 mm/h.

3. Global Hydrometeor Occurrence Statistics

[17] The statistics of various hydrometeor layer geometric properties are compiled using $1° \times 1°$ latitude-longitude grid boxes where occurrences of cloud bases and tops are

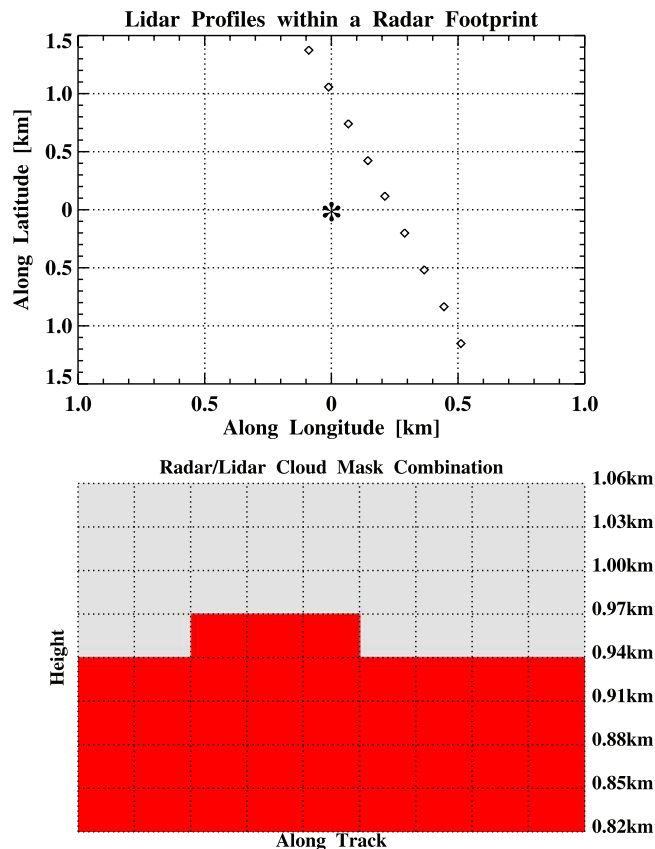Radar: Latitude = 18.06   Longitude = -85.96   Height = 0.94km   Bin = 101

Figure 3. The distribution of CALIOP measurements within a CPR resolution volume denoted by the circled area in Figure 1. (top) A plan view of the region illuminated by a CPR footprint centered on the asterisk and CALIOP (diamonds) footprints within the CRS footprint. (bottom) A vertical cross section of a CPR resolution volume (vertical bin 101) and the CALIOP volumes that observed cloud within the CPR volume (red). No radar echo was recorded in this sample volume.

counted during 1 month periods from the RL-GEOPROF data. In order to create reasonable statistics from the sparse sampling of the non scanning instruments, we compile seasonal or longer averages within $6° \times 8°$ grid boxes for most of the quantities shown. The occurrence frequency is calculated as the number of times a certain event occurs divided by the total possible number of times it could occur within the averaging period and region considered. Hereinafter we refer to this ratio as the coverage of a particular quantity.

3.1. Hydrometeor Coverage

[18] Perhaps the most basic statistic that we might consider is the global coverage of hydrometeors. The global coverage shown in Figure 5 is weighted by the cosine of the latitude to account for the surface area of the Earth. Also in Figure 5 we show the monthly time series of the cloud cover as derived from the MODIS cloud mask sampled along the Cloudsat-CALIPSO track. Overall, the global hydrometeor cover from the Cloudsat-CALIPSO data set averages 76% with an annual oscillation that peaks in October 2006 at a

value near 78% and reaches a minimum of 74% in March 2007. The MODIS cloud fraction tracks this tendency but is approximately 2% less than found by the active remote sensors. While these statistics are higher than reported from an analysis of the International Satellite Cloud Climatology Project (ISCCP) D-series data (68%) [*Rossow and Schiffer*, 1999], these results are similar to the coverage reported by *Wylie et al.* [1994] of 76.8% in their analysis of 4 years of HIRS data. One must keep in mind, however, the dependence of this quantity on the footprint size, sensitivities of the instruments, and data analysis methodologies that we use.

[19] In Figure 6, the zonally averaged coverage is presented in terms the top and base heights of hydrometeor layers. In Figure 6a, only the highest top contributes to the statistics, while in Figure 6b, all occurrences of a layer with the indicated base height are counted. The coverage fractions of low (tops < 3 km), middle (tops between 3 and 6 km), high (tops between 6 and 14 km) and what we term Tropopause Transition Layer cirrus (TTL; tops > 14 km and layer thickness less than 3 km) are additive and produce the overall zonal coverage in Figure 6a. The contrast between the layer top versus layer base depictions is intriguing. Where, in Figure 6b, we find that low-based clouds are the predominant cloud type contributing to the majority of clouds on Earth; layers with low-level tops have a roughly similar contribution to the total occurrence. These cloud type characteristics have substantial implications for the radiative energy balance of the climate system since layer top-based statistics are most closely associated with the infrared emission to space while the layer-based statistics have significant implications for the infrared cloud forcing at the surface.
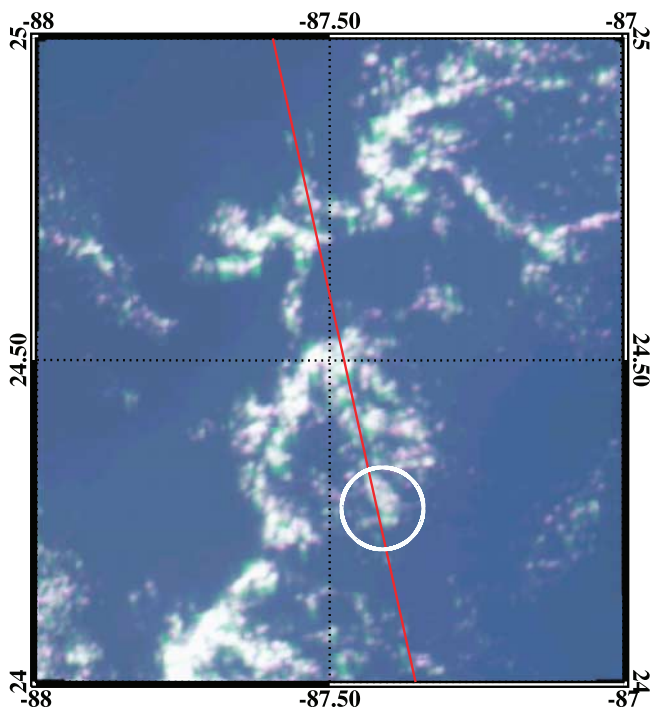

Figure 4. As in Figure 1 except data were collected over the southern Gulf of Mexico. The ER2 was not present along this track.
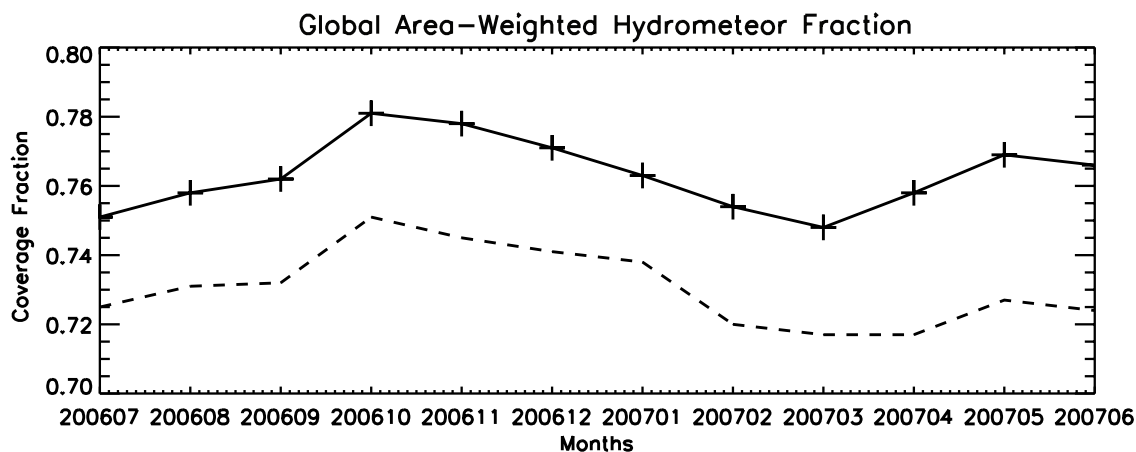
Figure 5. Monthly hydrometeor coverage fraction derived from the merged Cloudsat-CALIPSO data (solid curve) and from the MODIS cloud mask sampled along the Cloudsat-CALIPSO track.

[20] While we do not segregate in this analysis by season or land versus ocean, Figure 6b is broadly consistent with the analysis compiled from surface observer reports presented by *Warren et al.* [1988]. Cloudsat and CALPSO are uniquely suited to examining layer base statistics. However, the majority of our knowledge of cloud distributions comes from satellite data sets that characterize occurrence in terms of the radiometric layer top. Figure 7 shows a comparison of cloud top statistics from December, January, and February (DJF) of 2006 and 2007 to other compilations. The ISCCP and Clouds and the Earth's Radiance Energy System (CERES) values are adapted from *Zhang et al.* [2005, Figure 1] and use various DJF periods as described therein. Our low, middle, and high cloud height-based definitions correspond roughly to the pressure-based definitions (low, top pressure > 680 mb and high, top pressure < 440 mb) used by ISCCP and Zhang et al.

[21] While the high cloud statistics in Figure 7a are in reasonably good agreement with the SAGE II analysis by *Liao and Rossow* [1995, Figure 3], Cloudsat and CALIPSO record substantially more high-topped layers than derived from the passive remote sensing data sets shown here. This is true at nearly all latitudes except when thin TTL clouds are excluded from the Cloudsat/CALIPSO high cloud coverage (dashed curve in Figure 7a). When thin high clouds above 14 km are not counted, agreement is found with ISCCP in the tropics. Part of the difference between the active and passive measures of high clouds is likely accounted for in the middle-level clouds where the ISCCP and CERES find more middle-topped layers than Cloudsat and CALIPSO. There is a well known tendency for passive algorithms to place optically transmissive cirrus in the middle troposphere as discussed by *Zhang et al.* [2005] and elsewhere. Very good agreement is found with ISCCP at all latitudes and CERES equatorward of 40° for low-topped clouds.

[22] Further detail regarding the zonal distribution of hydrometeors is shown in Figure 8 where the zonally averaged occurrences are considered as a function of height. Figure 8 can be compared to Figure 3 of *Mace et al.* [2007] and illustrates the importance of including the CALIPSO lidar statistics to get a full picture of the hydrometeor

occurrence statistics. Well known features of the general circulation can be readily identified in Figure 8 including the inter tropical convergence zone (ITCZ) and associated maxima in upper tropospheric clouds, the descending branches of the Hadley Cells, as well as the predominance of the low-level clouds in the middle-latitude storm tracks, especially in the Southern Ocean. The patterns and occurrence frequencies in Figure 8 can be compared with the zonal mean quantities derived from ISCCP and shown by *Rossow et al.* [2005, Figure 4]. We tend to find more high-level clouds in the tropics yet the agreement in the middle latitudes is very good.

[23] Figure 9 shows the overall geographic coverage of hydrometeors and can be compared to the total zonal hydrometeor coverage in Figure 6 and the zonal height distribution of hydrometeors in Figure 8. Cloud cover exceeding 90% is found at nearly all longitudes between 50°S and 70°S and within the storm tracks in the North Atlantic and North Pacific. Given the very uniform geographic distribution of cloudiness on Earth, it is actually easier to describe where clouds are unlikely such as over the continental deserts in the descending arms of the Hadley Cells. We focus hereafter on describing how this hydrometeor coverage is distributed vertically and as a function of layer thickness.

[24] Classifying by hydrometeor layer base height and layer thickness in Figures 10–13, we find that low-level layers (bases less than 3 km mean sea level) are predominant over the global oceans with coverage exceeding 80% in the north Pacific and Atlantic storm tracks and throughout the Southern Ocean (Figure 10). These cloudy regions extend equatorward along the west coasts of the continents where they are predominantly associated with marine stratocumulus layers that are geometrically thin. The subtropical oceans maintain an overall coverage of low-based clouds in the 40–50% range with a greater fraction of these layers being geometrically thin in the eastern Pacific, the Atlantic and the Indian Ocean west of Australia. These regions of low-based geometrically thin cloud regimes were identified by *Klein and Hartmann* [1993] where they examined regional differences in dynamics, thermodynamic stability, and radiative influence among the various cloud
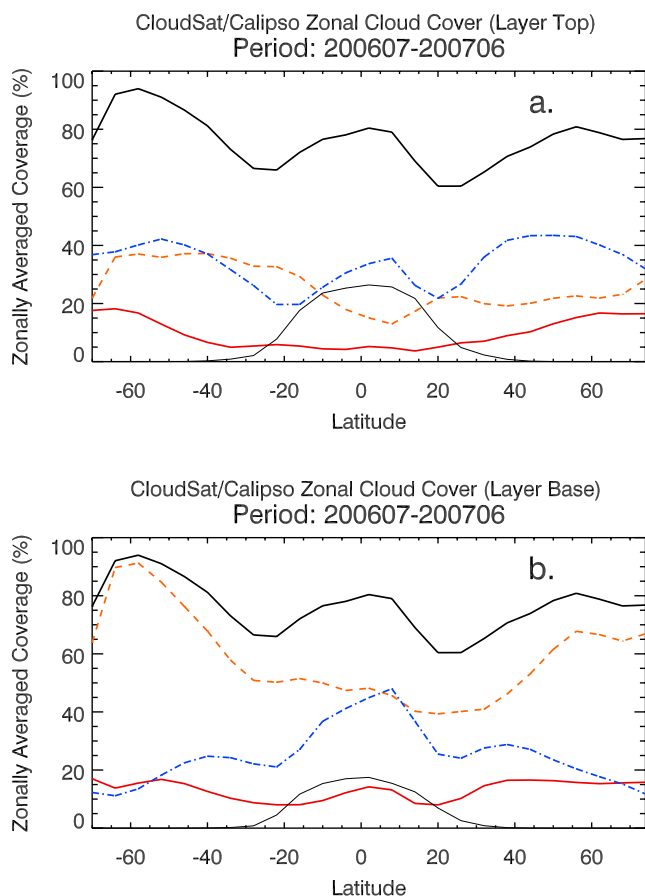
CloudSat/Calipso Zonal Cloud Cover (Layer Top)
Period: 200607-200706

a.

CloudSat/Calipso Zonal Cloud Cover (Layer Base)
Period: 200607-200706

b.

Figure 6. Zonally averaged hydrometeor coverage averaged in 2° latitude bins. (a) Type is defined by layer top altitude. (b) Type is defined by layer base altitude. The averaging period is from July 2006 through June 2007. The thick solid curve includes all hydrometeor layers. The blue dashed curves show coverage of layers with tops (bases) below 3 km mean sea level. The thin solid red curves shows layers with tops (bases) between 3 and 6 km, the dash-dotted blue curves show layers with tops (bases) between 6 and 14 km, and the thin solid black curves show layers with tops (bases) above 14 km. Multiple layers are counted in Figure 6b, but only the highest top is counted in Figure 6a. In Figure 6a the thin black curve counts only layers with tops above 14 km and that have thickness less than 3 km.

regions using satellite data and surface observer reports. Geometrically thin layers are relatively less common over the oceanic storm tracks and the convective regions of the western Pacific warm pool where low-based deep layers (thickness greater than 6 km) have a greater relative coverage. One must keep in mind also that these results are derived from averaging observations collected at approximately 1330 and 0130 local time over a full annual cycle. These local times are not coincident with diurnal convection maxima over the tropical oceans (∼0500) or the continents (∼1700).

[25] Middle-level clouds (defined as having bases from 3 to 6 km) are much less common than clouds based below 3 km (note the shift in color bar in Figure 11). This is especially true over the subtropical ocean where middle-

level clouds are nearly totally absent in this region of large-scale subsidence. Layers based in this vertical interval appear to be more likely over the continents. Note also that over high elevations such as the Himalaya and the Rocky
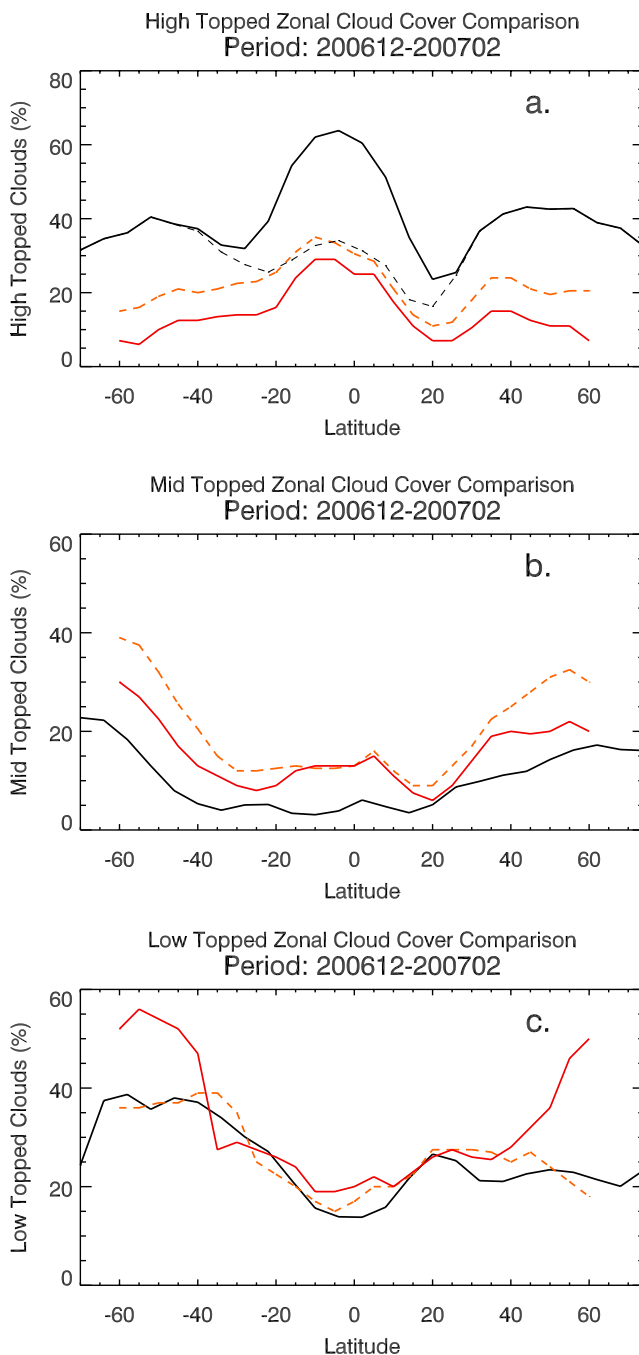

High Topped Zonal Cloud Cover Comparison
Period: 200612-200702

a.

Mid Topped Zonal Cloud Cover Comparison
Period: 200612-200702

b.

Low Topped Zonal Cloud Cover Comparison
Period: 200612-200702

c.

Figure 7. Comparison of Cloudsat/CALIPSO zonal coverage (solid black curve) defined as in Figure 6a with ISCCP (orange dashed curve) and MODIS-CERES (solid red curve) as adapted from *Zhang et al.* [2005, Figure 1]. The averaging period for Cloudsat/CALIPSO is December 2006 to February 2007. (a) High-topped layers, (b) middle-topped layers, (c) low-topped layers. In Figure 7a the black dashed curve excludes layers that have tops above 14 km and are less than 3 km thick.
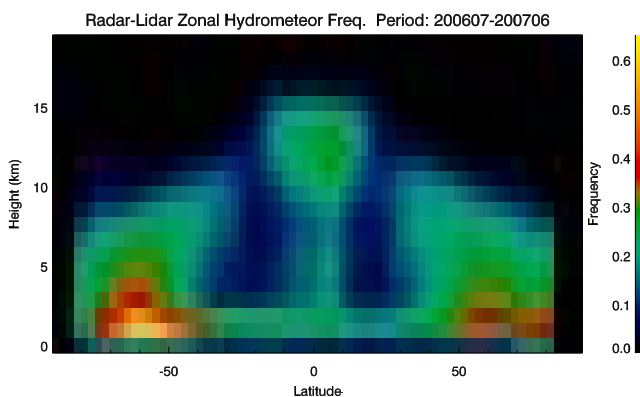
Figure 8. Zonally averaged vertical occurrence frequency in 2° latitude bins from the merged Cloudsat-CALIPSO data. The averaging period is from July 2006 through June 2007.

Mountains, the 3–6 km layer incorporates the elevated surface. The vast majority of these layers are geometrically thin (not shown) especially in the tropics while at higher latitudes, thicker layers are relatively more common although layers more than 6 km thick and midlevel based remain rare compared to layers in the other height ranges considered.

[26] The coverage of ice cloud layers with bases greater than 6 km, 6–10 km, 10–14 km, and greater than 14 km are shown in Figures 12 and 13. Upper tropospheric clouds are a predominant component of the cloud distributions in nearly all climate regimes although the sources of the clouds tend to vary with latitude and geography [*Sassen*, 2002]. A certain hemispheric symmetry is found where upper tropospheric layers associated with the subtropical jets occupy distinct pathways across the subtropical latitudes connecting the tropics and the middle latitudes, especially in the 10–14 km height range. The coverage in the 10–14 km layer is significantly greater than in the 6–10 km layer in the tropical latitudes, and at all latitudes, layers based in the 10–14 km layer tend to be geometrically thin except in the deep tropics. The majority of ice phase layers poleward of about 45° in both hemispheres are geometrically thin (not shown) with geometrically thicker layers being more prevalent at lower latitudes. Layers based above 6 km and more than 6 km thick are only found equatorward of 30° and are likely associated with outflows from deep convective systems (Figure 12b).

[27] The advantage of using layer base to classify cloud occurrence statistics is evident when comparing Figures 12 and 13 with Figure 14 where layer tops above 6 km are shown. The tropopause forms a natural barrier to the vertical development of most layers so that layer top statistics compiled from Cloudsat and CALIPSO largely map the latitudinal variation of tropopause height whereas cloud base is determined more by where the large-scale processes produce ascent and initial condensation. Since the layer top depiction includes layers that are deep and penetrate through much of the troposphere (especially in the mid latitude storm track regions), the connection to dynamical processes is largely lost. Figure 14 can also be compared directly to results in other satellite studies. For instance, *Jin*

et al. [1996] show cloud top statistics derived from ISCCP and HIRS for October 1989 (their Figures 5 and 6). The annual averages shown here have a similar pattern but tend to have a smaller overall coverage than HIRS but more than ISCCP.

[28] The very highest-based cirrus (bases above 14 km; see Figure 13c) consist almost entirely of geometrically thin layers that are too tenuous to be observed by the CPR on Cloudsat and are detected only by the CALIOP. These high-based clouds of the TTL have annually averaged coverage in excess of 20% in a broad region centered on the equator and bounded by about 25° in either hemisphere. We find a maximum in coverage from just east of the dateline to about 160°W that is nearly 30%. The statistics of the TTL cirrus shown here are similar to what has been reported previously using data from other satellites except that the peak occurrence region in the western Pacific is displaced east of where it has been found by limb viewing instruments in published reports [e.g., *Liu*, 2007; *Wang et al.*, 1996]. Further study and additional data will be required to determine if the weak El Niño that occurred during this period may be associated with this eastward displacement.

[29] The occurrences of very thick layers that have tops in the upper tropical troposphere and the TTL are also of interest since they signify the presence of deep convection (Figure 15). These cloud systems, while having a significant impact on the radiative balance of the region also release vast quantities of latent heat and can modify the properties of the TTL through direct injection of water vapor and condensate [e.g., *Dessler et al.*, 2007]. During this particular annual cycle during which a weak warm ENSO event occurred, the peak coverage of deep clouds was approximately 9% along the equator between about 140E and 170E. These coverage values are substantially greater than found using TRMM where deep convection is defined by the penetration of the 20 dBZ contour above 14 km [*Liu et al.*, 2007]. It is of interest to note also that the location of the peak in coverage of TTL cirrus (Figure 13c) is well removed and generally upstream of the peak occurrence
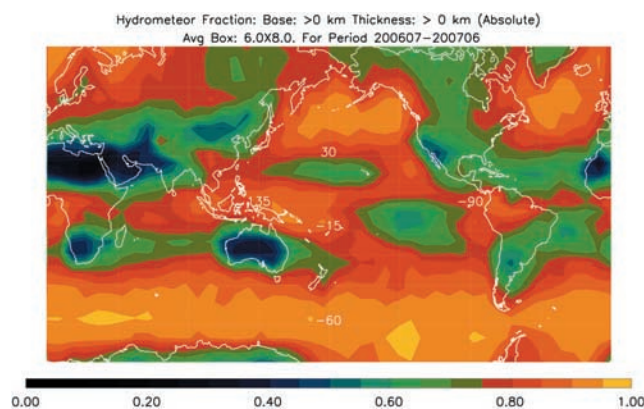

Figure 9. Hydrometeor coverage from the merged Cloudsat-CALIPSO data set where the total number of profiles containing at least one hydrometeor layer of any layer thicknesses is normalized by the total number of profiles. The averaging period is from July 2006 through June 2007 in 6 × 8° latitude-longitude averaging regions.

of deep convective cloud systems suggesting that much of the thin cirrus above 14 km has a formation mechanism that is not directly associated with deep convective injection.
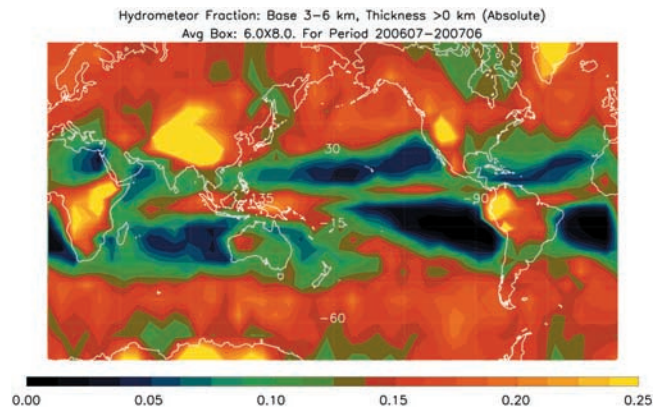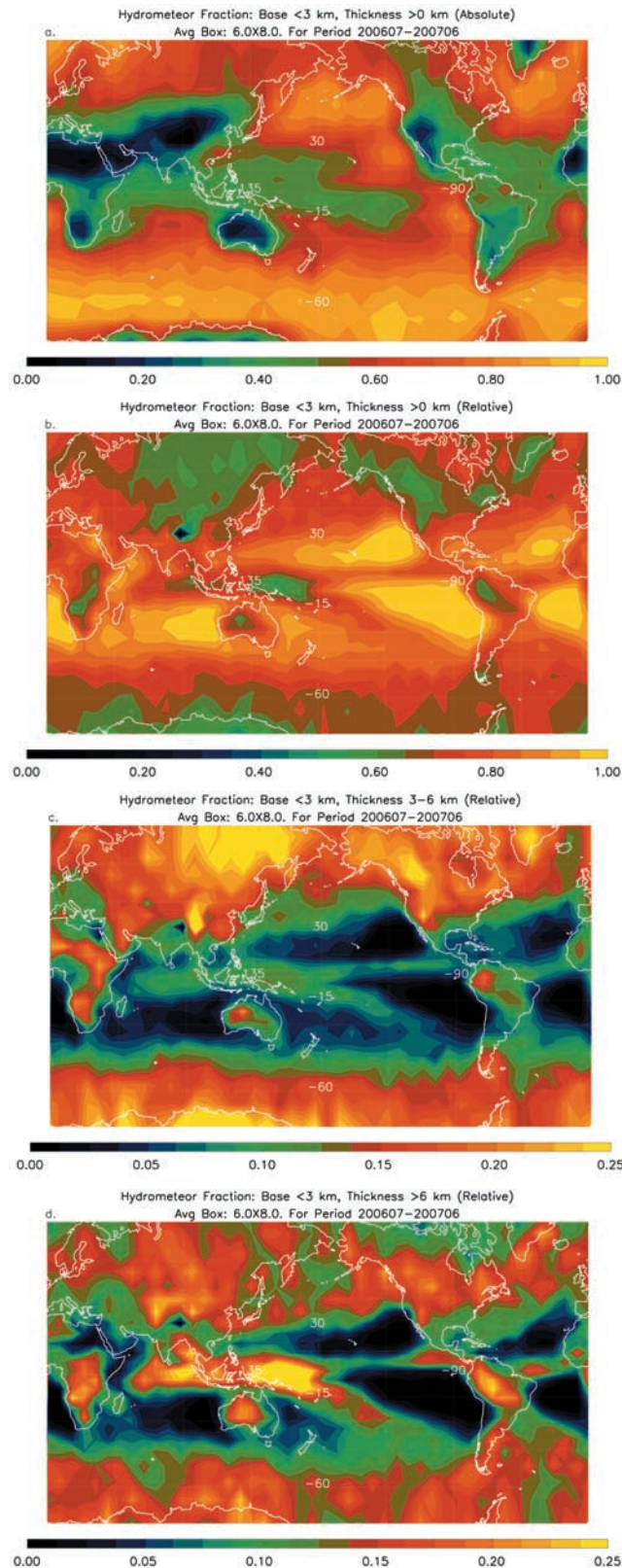

Figure 11. As in Figure 10a except that layers based between 3 and 6 km are considered.

3.2. Layer Thickness and Multiple Layers

[30] The cloud climatology of Earth, regardless of location, is dominated by geometrically thin hydrometeor layers as demonstrated in the zonally averaged frequency distribution of layer thickness in Figure 16 where we find a global mean layer thickness of approximately 3 km. This value of mean layer thickness is about a factor 2 greater than that reported by *Wang et al.* [2000] using an analysis of radiosonde mandatory and significant levels. The difference we find is likely related to our requirement that at least 1 km of hydrometeor-free air exist before an additional layer is identified although their use of mandatory and significant levels imposed a reasonably similar although not identical constraint. Probably more relevant is that the radar is inherently sensitive to large particles that can often fall well below local maxima in the humidity profile used by *Wang et al.* [2000] to identify cloud boundaries. This tendency for large particles to sediment below the regions of high humidity would also tend to cause otherwise separate cloud layers to be seen as a single layer in the radar data. These issues will require further study. We also miss some boundary layer clouds that exist below upper layer clouds with even moderate optical depths (greater than about 2−3), because the Cloudsat radar is generally unable to detect these clouds and the lidar becomes attenuated.

[31] We find that the peaks in layer thickness in the northern hemisphere are associated with maxima over the northern midlatitude continents while a more zonally smooth distribution of layer thickness is found around the Southern Ocean. The marine stratus and trade cumulus layers contribute to the minima in thickness at subtropical latitudes while oceanic convection of the ITCZ contributes

Figure 10. (a) Hydrometeor fraction of layers with base less than 3 km and any layer thicknesses. (b) As in Figure 10a except that layer thickness is less than 3 km and the fraction is relative to the quantity in Figure 10a. (c) As in Figure 10b except that layer thicknesses are between 3 and 6 km. (d) As in Figure 10b except that layer thickness is greater than 6 km. The averaging period is from July 2006 through June 2007 in $6 \times 8°$ latitude-longitude averaging regions.
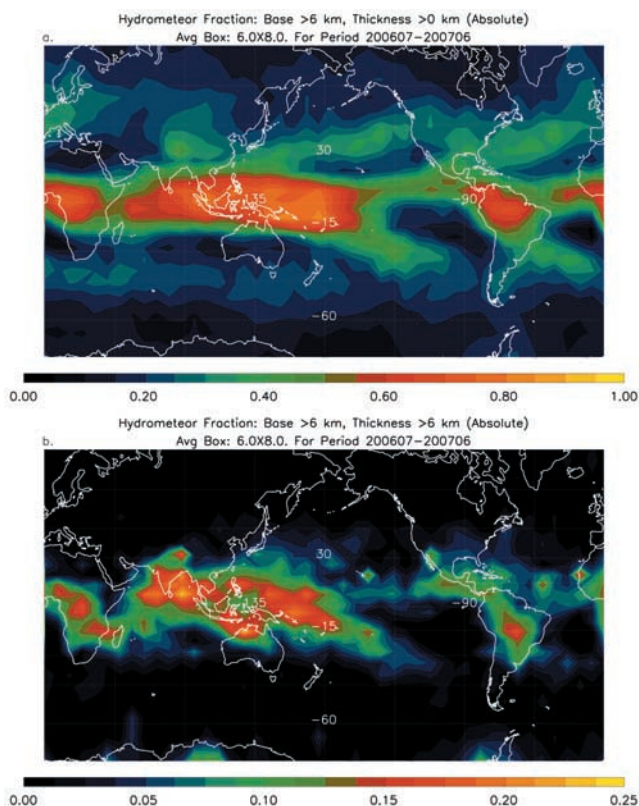
Figure 12. As in Figures 10a and 10b except that layers that have bases greater than 6 km are considered.

to the maxima in the tropics. The 12–15 km layer thickness occurrence maximum that is evident in the zonal average equatorward of 20° latitude is associated primarily with seasonal Asian and Australian monsoon convection and the annual migration of the ITCZ associated with the monsoons. Also contributing to this feature is land-based convection over South America and Africa. Although, again, we must emphasize the fact that the sun synchronous orbit does not adequately sample the diurnal cycle.

[32] The measurements by Cloudsat and CALIPSO are well suited for indentifying the presence of multiple cloud layers. Figure 17a shows the global distribution of the occurrence (relative to the frequency of all cloudy profiles shown in Figure 9) of multiple cloud layers where we define distinct layers by requiring a hydrometeor-free distance of 4 range bins (approximately 1 km) between the top of a lower layer and the base of the next highest layer. Globally, the occurrence of multiple layers is 24% while *Wang et al.* [2000] report a global multilayer occurrence of approximately 40%. This difference in multilayer occurrence is consistent with Wang et al. finding layers that are much thinner than we derive from the active remote sensors. Figure 17 shows that the occurrence of multiple layers is a strong function of latitude and geography with multiple layer occurrences over the tropical oceans exceeding 60% of all cloudy profiles such as in regions of the western Pacific and elsewhere in the ITCZ. The tropical multi layer fraction decreases to peak values of 45% if we exclude TTL cirrus from consideration. There seems also to be a tendency for multiple layers to be observed over tropical Africa and

South America. Multiple layers tend to occur more often over the storm tracks of the north Pacific than over the Southern Ocean. The marine stratus regions and subtropical latitudes in general where free tropospheric subsidence is strong (i.e., the descending branch of the Hadley Cells), tend also to be a region of minimum multiple layer occurrence – although we again recognize the radar's inability to detect low nondrizzling cumulus likely renders the values reported here somewhat low.

[33] The predominant cooccurrence of multiple hydrometeor layers is essentially dominated by low-based layers occurring with high-based layers over oceanic regions equatorward of 45° in each hemisphere (Figure 17c).
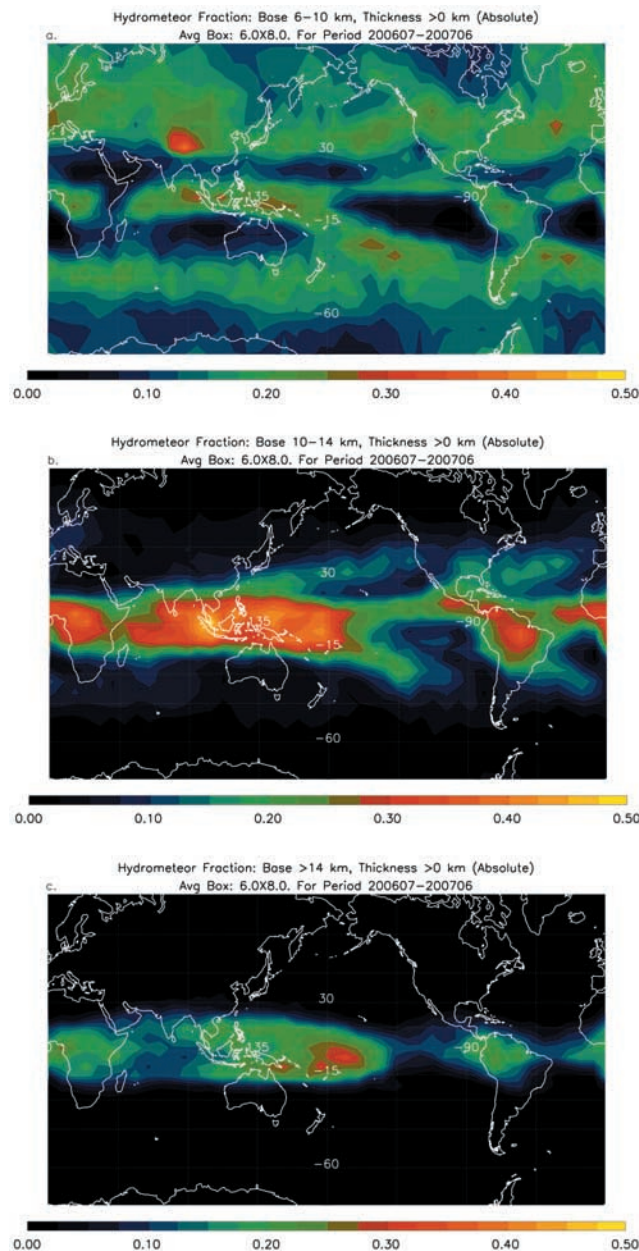

Figure 13. As in Figure 10a except that layers based between (a) 6 and 10 km, (b) 10–14 km, and (c) > 14 km are considered.
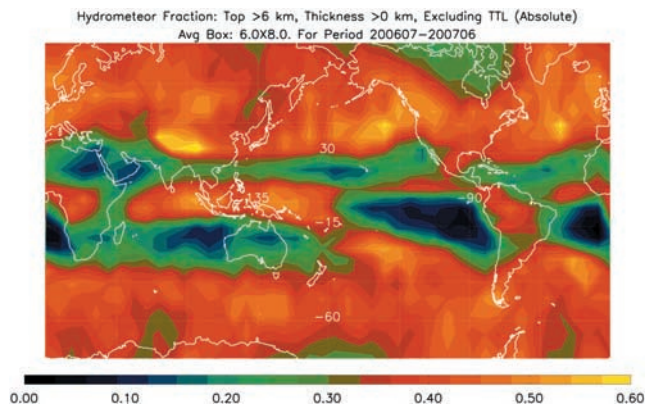
Figure 14. Coverage of layers with tops exceeding 6 km of all thicknesses excluding layers whose tops exceed 14 km with layer thickness less than 3 km. The averaging period is from July 2006 through June 2007 in 6 × 8° latitude-longitude averaging regions.

Poleward of these latitudes, multiple layer occurrence is predominantly low based with middle based (Figure 17b) while multiple low layers are observed in the high latitudes of the Southern Ocean (not shown). Interestingly, we note that the occurrence of mid level layers with high-based layers tends to be a continental phenomenon in addition to in the ITCZ of the western Pacific and Indian Oceans (Figure 17d). Multiple high-based layers tend to occur primarily over the tropical oceans and over the subtropical continents.

[34] It is difficult to rectify these results in their present form with the seminal cloud climatology of *Warren et al.* [1986]. Their analysis of surface observer reports is presented in terms of contingency probabilities of observer-defined cloud types while we have derived relative frequencies of occurrence. Surface observers will report the occurrence of layers in the visible sky that extends from horizon to horizon while we analyze layer cooccurrence from strictly defined vertical profiles. What does appear consistent between the two data sets is the predominance of cirrus and low-level clouds over the middle- and low-latitude oceans. On the other hand their analysis does not appear to
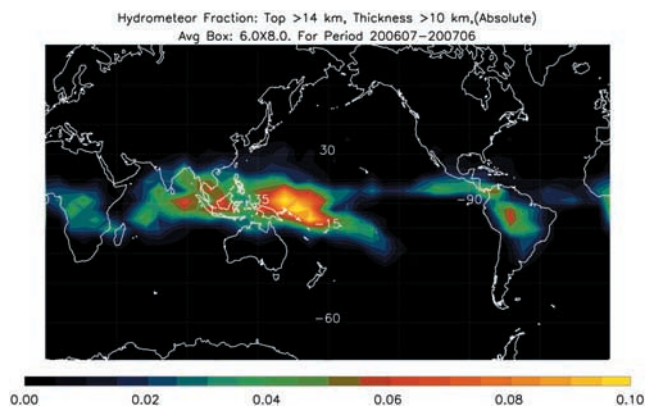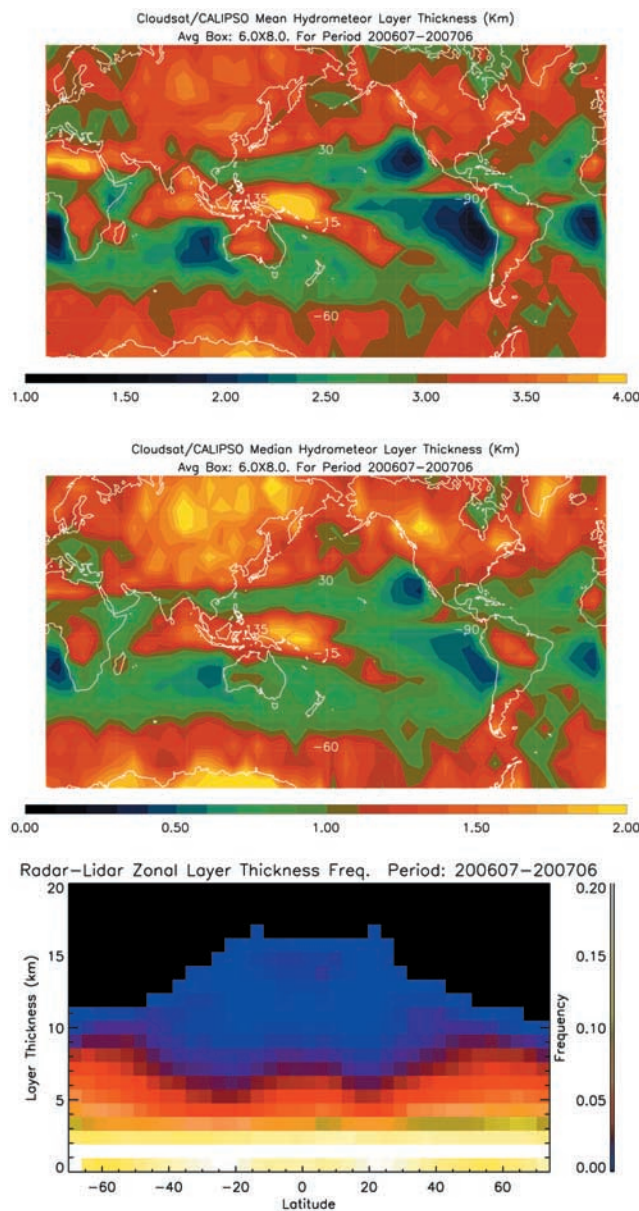

Figure 16. Hydrometeor (top) mean and (middle) median layer thickness and (bottom) the zonal layer thickness frequency distribution of all layers observed from July 2006 through June 2007 in 6 × 8° latitude-longitude averaging regions.

identify the occurrence of middle level with high clouds over the continents. Further work will be required to fully understand the similarities and differences between these two data sets.

[35] A persistent question regarding existing satellite-based climatologies that use passive radiometric techniques, is the degree to which high-level clouds obscure lower-level layers. While this issue can best be examined using estimates of high-layer optical depth, we present in Figure 18, the occurrence of geometrically thick (layer thickness greater than 3 km) and high-topped (>6 km) layers with distinct lower-level layers whose tops are lower than 6 km. We find that the peak cooccurrence of such layers are generally less than 10% with maxima in regions of deep convection in the
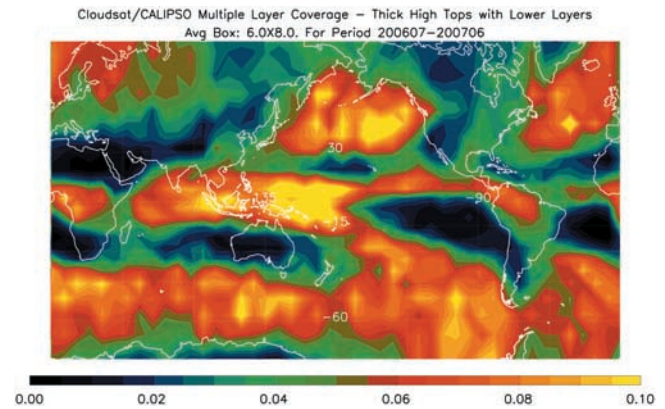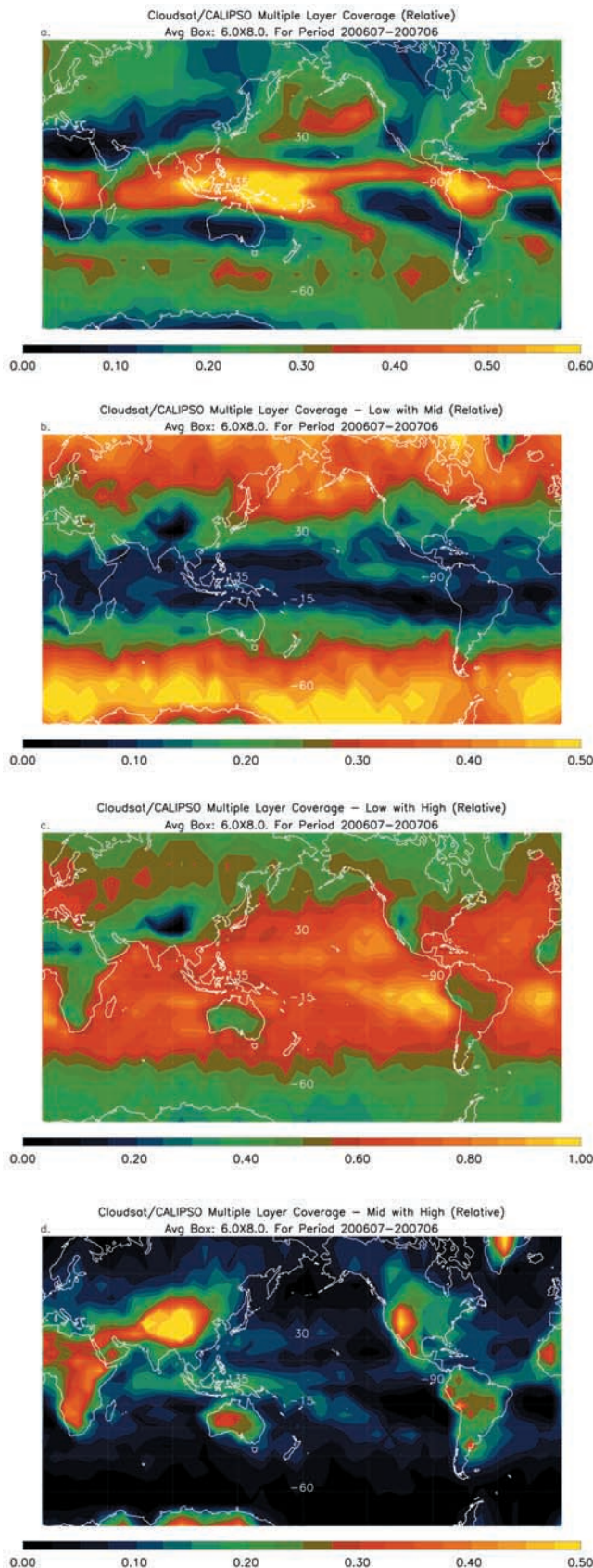

Figure 15. Coverage of layers whose tops exceed 14 km and with thicknesses exceeding 10 km.

Figure 18. The coverage of layers with tops less than 6 km of all thicknesses that occur with layers that have tops greater than 6 km and layer thickness greater than 3 km.

tropical western Pacific and in the ITCZ generally. The maritime mid latitude storm track regions in both hemispheres are also favored locations for this phenomenon.

4. Hydrometeor Layer Overlap Properties

[36] As discussed in several recent papers [*Pincus et al.*, 2005; *Barker et al.*, 1999; *Hogan and Illingworth*, 2000], the representation of fractional overlap of simulated cloud layers in coarse resolution models has significant bearing on the radiative properties of a model grid box at a particular instant in time and ultimately on the manner by which the model achieves radiative balance. In this discussion we use the term layer as meaning the entire cloud layer from base to top while we use the term sublayer to mean some vertical interval (i.e., the vertical spacing of a model layer) that encompasses some fraction of a cloud layer. Cloud overlap typically refers to the relationship between the cloud fractions in two distinct sublayers on some spatial scale. Consider, for instance, that two cloud sublayers that each have a fractional coverage of 0.5 can, when overlapped minimally, cause the domain to be fully overcast. On the other hand, when those sublayers are overlapped maximally, the domain will have a fractional coverage of 0.5. One can also define situations where sublayers are randomly overlapped. It is typically assumed that two cloudy sublayers

Figure 17. Multiple layer coverage. (a) The coverage of multiple layers from the merged Cloudsat-CALIPSO data set where the total number of multiple layer profiles (defined as a profile with a 1 km hydrometeor-free space between range volumes that contain hydrometeors) are normalized by the total number of profiles. (b) As in Figure 17a except that the number of events of low-based layers (base < 3 km) occurring with middle-based layers (base 3–6 km) are normalized by the total number of multiple layers. (c) As in Figure 17b except that low-based layers occurring with high-based layers (layer base > 6 km) are shown. (d) As in Figure 17b except that middle-based layers occurring with high-based layers are shown. The averaging period is from July 2006 through June 2007 in 6 × 8° latitude-longitude averaging regions.
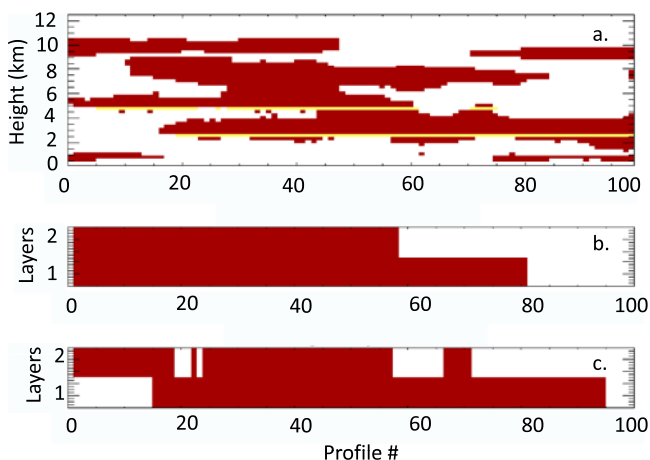
Figure 19. Example of fractional overlap analysis procedure. (a) Cloud mask cross section over the Southern Ocean. (b) The coverage of the sublayers shown in yellow in Figure 19a, assuming maximum overlap. (c) The actual coverage of the yellow sublayers. The actual coverage of the sublayers is 0.95. The coverage assuming maximum overlap is 0.81, and the coverage assuming random overlap is 0.92. The yellow range bins show the sublayers analyzed for their overlap characteristics in Figures 19b and 19c.

that are separated by clear air are randomly overlapped in their fractional coverage meaning that there is no correlation in the fractional coverage of the sublayers, while two sublayers that are part of a vertically contiguous cloud layer are assumed to be maximally overlapped [*Geleyn and Hollingsworth*, 1979].

[37] Cloud overlap has been examined recently using spaced-based lidar [*Dessler et al.*, 2006] and by analyzing time series of ground-based millimeter radar data [*Naud et al.*, 2007; *Mace and Benson-Troth*, 2002]. It has been found, as typically assumed in current GCMs that cloud layers separated by clear air tend to be randomly overlapped. We have found similar results in the Cloudsat-CALIPSO data considered globally over this annual cycle. However, this finding does not preclude the possibility that certain cloud cooccurrences would be correlated in some way under some meteorological circumstances as hypothesized by *Chen et al.* [2000]. Analysis of the fractional overlap properties as a function of layer cooccurrence and meteorology is a topic of future work. On the other hand, analysis of ground-based cloud radar data has shown that fractional overlap of sublayers that are part of a contiguous cloud layer are not necessarily well approximated by an assumption of maximum overlap. The degree of maximal overlap of sublayers of a contiguous layer tends to be a function of location, time of year, and the distance separating the two sublayers. It should also be noted that the quantitative results also tend to be a function of the assumption of the time or distance over which the data are averaged and the depth that is used to define the sublayers as shown by *Hogan and Illingworth* [2000] and *Mace and Benson-Troth* [2002] although the qualitative interpretation of the results remain consistent regardless of these specifications over a reasonable range of the sublayer

depth and averaging time as also found in the ground-based radar analysis.

[38] The merged Cloudsat-CALIPSO data are used to analyze the overlap characteristics of contiguous cloud layers globally in a manner similar to that first used by *Hogan and Illingworth* [2000] and later used by *Mace and Benson-Troth* [2002] and *Naud et al.* [2007] with the exception that along-track distance is substituted for time averages and the results are aggregated over some period of time in spatial averaging regions. In this technique, an along-track length (Δx) is specified over which the fractional cloud cover is determined over some depth (Δz) that forms the sublayer of a contiguous hydrometeor layer that can extend over several (2 or more) sublayers of depth Δz. By cloud cover, we mean the number of profiles along Δx that report hydrometeors in any Cloudsat resolution volume within the vertical interval of the sublayer Δz (see Figure 1 of *Mace and Benson-Troth* [2002] for an illustration). This number of cloudy profiles in the sublayer is divided by the total number of profiles along Δx. This fraction, if less than 1, is compared to other similarly defined sublayers that comprise the hydrometeor layer along the length Δx. From this comparison, the total hydrometeor coverage of the two combined sublayers is determined. This is what we define as the true coverage or C_{true}. From the individual coverages of the two sublayers, a cloud cover assuming maximal overlap is determined (C_{max}) and a cover assuming minimal overlap is determined (C_{min}). From these two assumed extremes, the random coverage can be determined (C_{ran}) as well as a parameter α that describes the degree to which the two layers are maximally overlapped according to,

$$C_{true} = \alpha C_{max} + (1 - \alpha)C_{ran}.$$

[39] In Figure 19 we present an example of this analysis procedure applied to two sublayers from a 100 profile segment collected over the Southern Ocean in July 2006. In this example, where we use $\Delta z = 240$ m (i.e., 1 range bin) for simplicity, we find a complicated cloud layer structure composed of multiple horizontally extended layers at several levels in this domain. The two yellow-shaded sublayers are evaluated for their overlap characteristics. Figure 19b shows how these layers would cover the domain if maximum overlap were assumed, and Figure 19c shows the actual coverage of the domain by these two sublayers. While the overlap assumption does not change the *volume* of the domain filled by these two sublayers, the fraction of the layer that is vertically covered by the sublayers is certainly influenced by the overlap assumption. The bias in the radiative properties due to the overlap assumption would be to cause higher overall optical depth and albedo in the portion of the grid box covered by clouds yet result in too little coverage overall. Interestingly, this bias is found by *Zhang et al.* [2005] in their comparison of GCM-simulated clouds and cloud forcing to satellite data. Since the radiative transmission is not a linear function of optical depth, these biases, while having an opposite sign, would not cancel and would result in an overall positive cloud albedo bias and excessive shortwave cloud forcing as also found by *Zhang et al.* [2005]. This radiative bias error would need to be accounted for through other compensating errors in the simulated atmosphere for the model to achieve radiative balance at the TOA and still agree with TOA radiative constraints. This point is made by *Barker et al.*
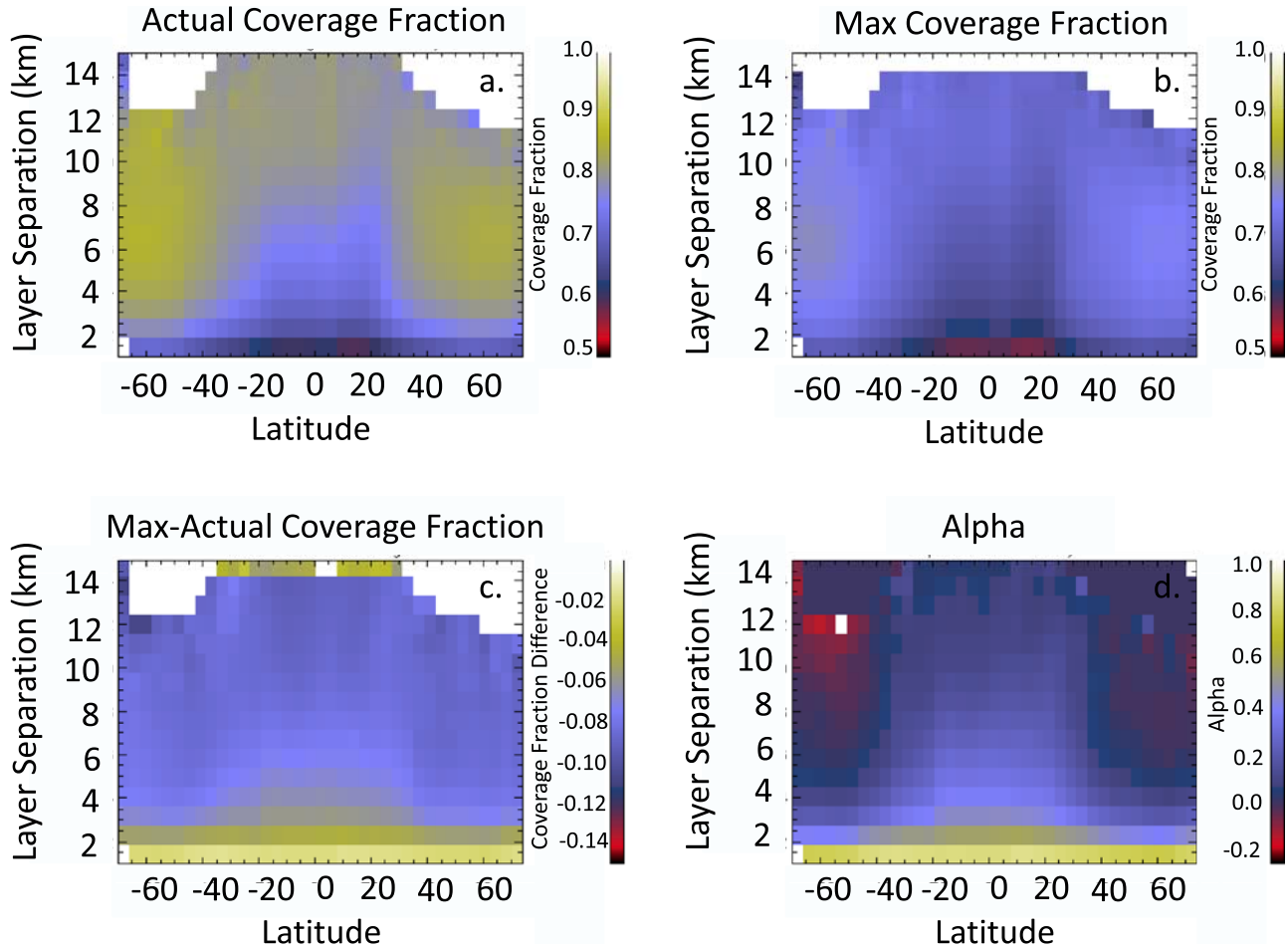
Figure 20. Zonal mean and annually averaged fractional overlap characteristics. (a) The mean true coverage of sublayers separated by the distances shown on the ordinate. (b) The coverage as a function of sublayer separation assuming maximum overlap of the sublayers. (c) The difference of the maximum and true coverage. (d) The mean overlap parameter α as described in the text.

[1999] and also explored in some depth by *Chen et al.* [2000], who found small TOA and Surface forcing errors yet substantial errors in atmospheric heating due to the overlap assumption in ISCCP.

[40] The zonally averaged overlap characteristics of vertically contiguous layers are shown as a function of sublayer separation in Figure 20 where we define $\Delta z = 1.0$ km (4 range bins) and $\Delta x = 200$ km (100 Cloudsat footprints). The results are similar to what has been reported previously using ground-based cloud radar data at various sites in the midlatitudes, tropics, and Arctic [*Mace and Benson-Troth*, 2002; *Naud et al.*, 2007]. An assumption of C_{max} tends to become an increasingly poor approximation of C_{true} as the latitude and sublayer separation increases. In the tropics where wind shears tend to be weaker and the occurrence of cloudiness is related to local convective scale processes where the vertical motion on the cloud system scale is large, we find that sublayers remain approximately maximally overlapped through a deeper layer. We should note, also, that precipitation, which we are not attempting to remove from this data, will tend to skew the results toward maximal overlap so these results should be considered a lower limit of the actual difference between C_{max} and C_{true}. Poleward of

30° in both hemispheres, the influence of vertical wind shear and synoptic-scale vertical motions that are less influenced by convective processes result in sublayers becoming less and less maximally overlapped for a given sublayer separation. There is evidence that in the Southern Ocean storm track regions the deepest layers are trending toward random overlap (Figure 20d). These results imply that the maximal overlap of contiguous layers assumed in many models will result in a global negative cloud fraction bias. This bias error is expressed in terms of a zonal average and sublayer separation in Figure 20c.

[41] By weighting the sublayer separation fractional bias error (shown as a zonal average in Figure 20c) with the frequency distribution of layer thickness (shown as a zonal average in Figure 16c) we approximate the error that a model with the spatial dimensions of our assumed vertical and horizontal separations would incur for layers that are vertically contiguous and non overcast were that model to correctly predict fractional cloudiness and the distribution of layer thicknesses as observed by Cloudsat and CALIPSO for those vertically contiguous and non overcast layers. Figure 21 illustrates that the bias error would be a strong function of climate regime. The negative bias error would
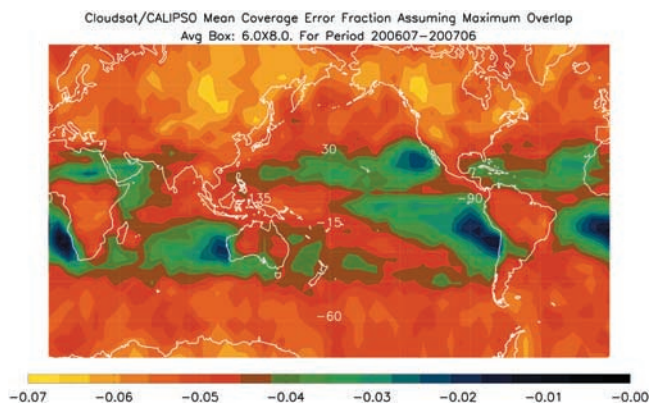
Figure 21. The annually averaged mean error from the actual coverage that would occur by assuming maximum overlap of all nonovercast vertically contiguous layers.

be greatest (∼6–7%) in the middle to high continental latitudes of the Northern Hemisphere and least in the subtropics where layers tend to be thin near the western coasts of the continents into the subtropical ocean basins dominated by trade cumulus. Much of the tropical latitudes experience negative fractional bias errors on the order of 4–5% where convection and relatively weak vertical wind shear causes layers to be more maximally overlapped. Interestingly, the high latitudes over Asia and North America experience the largest bias errors due to the significantly greater layer thicknesses that are observed there (Figure 15) compared to the Southern Ocean regions although the bias error over the Southern Ocean is larger for a given sublayer separation.

5. Summary and Discussion

[42] A data set combining the cloud masks from the millimeter radar on Cloudsat and the lidar on CALIPSO has been created and made publicly available. This combination of data allows us to resolve in unprecedented detail the vertical structure of hydrometeor layers ranging from optically thin cirrus and boundary layer clouds to deep optically thick precipitating systems. We have presented a broad initial analysis of the hydrometeor climatology created from the first year of this merged data set concentrating on three fundamental aspects: (1) the geographic distribution of hydrometeor layers as a function of layer base, top, and geometric layer thickness; (2) the occurrence of multiple layers and the relative cooccurrence of various layer types; and (3) the fractional overlap characteristics of hydrometeor sublayers. It is important to keep the limitations of the Cloudsat-CALIPSO data set in mind when considering the findings of this study. Most significantly, the CPR is unable to distinguish clouds from precipitation. While liquid precipitation can be identified with some precision [*Haynes and Stephens*, 2007], elevated precipitation and snow are more challenging. In this analysis we have not attempted to filter the data in any way.

[43] The cloud climatology of the Earth is dominated by geometrically thin layers based in the marine boundary layer. These clouds extend from the storm tracks of the middle and high latitudes to the trade cumulus zones of the subtropical latitudes and into the stratocumulus regimes west of the continental landmasses in both hemispheres [*Klein and Hartmann*, 1993]. Because of their high albedo over an otherwise dark ocean surface, marine boundary layer clouds are known to play a major role in regulating the Earth's climate. However, these clouds have been identified as a primary source of climate model uncertainty [*Bony et al.*, 2006]. It seems evident that the Cloudsat-CALIPSO data set combined with other data from the A-Train will allow for greater understanding of the coupling between these clouds and the atmosphere and ocean.

[44] On the other end of the radiative forcing spectrum, ice clouds of the upper troposphere (cloud base above 6 km) extend along the ITCZ where they have a maximum coverage of more than 60% over the western Pacific warm pool region into the middle latitudes along the climatological subtropical jet stream pathways. Ice clouds are predominantly geometrically thin (thicknesses less than 3 km) especially at middle and high latitudes as has been found from long-term ground-based measurements [*Sassen and Campbell*, 2001; *Mace et al.*, 2006]. Vertically extended ice clouds (thicknesses > 3 km) based above 6 km are not uncommon in the tropics where they are more likely associated with outflows from deep convection. On the other hand, geometrically thin cirrus with bases above 14 km are shown to occur throughout the global tropics with distinct minima in occurrence in the eastern Pacific and western Atlantic Oceans. We have found that during the annual cycle considered here during which a weak El Niño caused anomalous warming in the equatorial central Pacific, the occurrence of cirrus with bases above 14 km had a maximum in coverage just east of the dateline well removed from the peak occurrence of deep high-topped clouds that occurred between 140°E and 170°E.

[45] The occurrence of multiple layers has a global maximum in the tropical western Pacific and over equatorial South America and Africa where two or more layers are found to occur in more than 60% of all cloud profiles. The middle-latitude oceanic storms tracks in both hemispheres are also favored areas for multiple layer occurrences. The types of clouds that cooccur appear to depend on whether the occurrence is over land or ocean. Over the tropical ocean, the predominant multiple layer occurrences are cirrus over boundary layer clouds while over the maritime storm tracks, low-level layers tend to occur with middle-level clouds. However, over the continents, the predominant multiple layer cloud occurrence type is middle-level clouds existing with cirrus.

[46] While the occurrence and location of hydrometeors in a vertical column substantially influence the radiative properties of that column, the manner in which the vertical structure is represented in coarse resolution atmospheric models also has a significant bearing on whether the radiative properties are accurately characterized even when the fractional occurrence is accurately predicted in each vertical model level. The merged active remote sensor data is well suited for examining this issue and we find, as has been inferred from ground-based data, that the overlap characteristics trend toward random as sublayers become separated vertically. For the thickest layers over the storm tracks where vertical motions tend to be weak and wind

shear is large, layers become randomly overlapped. The negative bias error assuming correct cloud fraction prediction of a model with a horizontal resolution of approximately 180 km and a vertical interval of approximately 1 km ranges from near zero in the subtropics to as much as $6-7\%$ over the northern mid latitude continents for non overcast and vertically contiguous layers. A negative bias error of $4-5\%$ is found over most of the tropics with maxima over equatorial South America and Africa. An assumption of maximum overlap over the Southern Ocean storm tracks would result in negative bias errors of $5-6\%$.

[47] This paper represents an initial survey of the first annual cycle of merged Cloudsat-CALIPSO data that combines day and night measurements. As such, our purpose has been to illustrate the potential of this data to address fundamental issues facing the climate modeling community today. It is clear that we have entered a new era in global cloud observations where many of the previous uncertainties inherent in characterizing cloud occurrence and cloud properties with passive sensors or ground-based observers have been totally bypassed. With these active remote sensors, we now have very precise knowledge of the occurrence and vertical structure of hydrometeor layers and layer properties along the ground track of the instruments at the particular times of the measurements.

References

Ackerman, S. A., K. I. Strabala, W. P. Menzel, R. A. Frey, C. C. Moeller, and L. E. Gumley (1998), Discriminating clear sky from clouds with MODIS, *J. Geophys. Res.*, 103, 32,141–32,157, doi:10.1029/1998JD200032.

Barker, H. W., G. L. Stephens, and Q. Fu (1999), The sensitivity of domain-averaged solar fluxes to assumptions about cloud geometry, *Q. J. R. Meteorol. Soc.*, 125, 2127–2152.

Bony, S., et al. (2006), How well do we understand and evaluate climate change feedback processes?, *J. Clim.*, 19, 3445–3481, doi:10.1175/JCLI3819.1.

Chen, T., W. B. Rossow, and Y. Zhang (2000), Radiative effects of cloud-type variations, *J. Clim.*, 13, 264–286, doi:10.1175/1520-0442(2000)013<0264: REOCTV>2.0.CO;2.

Dessler, A. E., S. P. Palm, and J. D. Spinhirne (2006), Tropical cloud-top height distributions revealed by the Ice, Cloud, and Land Elevation Satellite (ICEsat)/Geoscience Laser Altimeter System (GLAS), *J. Geophys. Res.*, 111, D12215, doi:10.1029/2005JD006705.

Dessler, A. E., T. F. Hanisco, and S. Fueglistaler (2007), Effects of convective ice lofting on H$_2$0 and HDO in the tropical tropopause layer, *J. Geophys. Res.*, 112, D18309, doi:10.1029/2007JD008609.

Geleyn, J. F., and A. Hollingsworth (1979), An economical analytical method for the computation of the interaction between scattering and line absorption of radiation, *Contrib. Atmos. Phys.*, 52, 1–16.

Haynes, J. M., and G. L. Stephens (2007), Tropical oceanic cloudiness and the incidence of precipitation: Early results from Cloudsat, *Geophys. Res. Lett.*, 34, L09811, doi:10.1029/2007GL029335.

Haynes, J. M., T. S. L'Ecuyer, G. L. Stephens, S. D. Miller, C. Mitrescu, N. B. Wood, and S. Tanelli (2009), Rainfall retrieval over the ocean with spaceborne W-band radar, *J. Geophys. Res.*, 114, D00A22, doi:10.1029/2008JD009973.

Hogan, R. J., and A. J. Illingworth (2000), Deriving cloud overlap statistics from radar, *Q. J. R. Meteorol. Soc.*, 126, 2903–2909, doi:10.1002/qj.49712656914.

Im, E., S. L. Durden, and C. Wu (2005), Cloud profiling radar for the Cloudsat mission, *IEEE Trans. Aerosp. Electron. Syst.*, 20, 15–18, doi:10.1109/MAES.2005.1581095.

Jin, Y., W. B. Rossow, and D. P. Wylie (1996), Comparison of high-level clouds from HIRS and ISCCP, *J. Clim.*, 9, 2850–2879, doi:10.1175/1520-0442(1996)009<2850:COTCOH>2.0.CO;2.

Klein, S. A., and D. L. Hartmann (1993), The seasonal cycle of low stratiform clouds, *J. Clim.*, 6, 1587–1606, doi:10.1175/1520-0442(1993)006<1587:TSCOLS>2.0.CO;2.

Li, L., G. M. Heymsfield, P. E. Racette, and L. Tian (2004), A 94 GHz cloud radar system on a NASA high-altitude ER-2 aircraft, *J. Atmos. Oceanic Technol.*, 21, 1378–1388.

Liao, X., and W. B. Rossow (1995), Comparison between SAGE II and ISCCP high-level clouds: 1. Global and zonal-mean cloud amounts, *J. Geophys. Res.*, 100, 1121–1135, doi:10.1029/94JD02429.

Liu, C. (2007), Geographical and seasonal distribution of tropical tropopause thin clouds and their relation to deep convection and water vapor viewed from satellite measurements, *J. Geophys. Res.*, 112, D09205, doi:10.1029/2006JD007479.

Liu, C., E. J. Zipser, and S. W. Nesbitt (2007), Global distribution of tropical deep 9 convection: Different perspectives from TRMM infrared and radar data, *J. Clim.*, 20, 489–503.

Liu, Z., M. A. Vaughan, D. M. Winker, C. A. Hostetler, L. R. Poole, D. Hlavka, W. Hart, and M. McGill (2004), Use of probability distribution functions for discriminating between cloud and aerosol in lidar backscatter data, *J. Geophys. Res.*, 109, D15202, doi:10.1029/2004JD004732.

Mace, G. G., and S. Benson-Troth (2002), Cloud overlap characteristics derived from long-term cloud radar data, *J. Clim.*, 15, 2505–2515, doi:10.1175/1520-0442(2002)015<2505:CLOCDF>2.0.CO;2.

Mace, G. G., S. Benson, and E. Vernon (2006), On the relationship between cirrus cloud occurrence and microphysical properties with the large-scale atmospheric state revealed by 6 years of continuous ground-based cloud radar data, *J. Clim.*, 19, 3257–3278, doi:10.1175/JCLI3786.1.

Mace, G. G., R. Marchand, Q. Zhang, and G. Stephens (2007), Global hydrometeor occurrence as observed by Cloudsat: Initial observations from summer 2006, *Geophys. Res. Lett.*, 34, L09808, doi:10.1029/2006GL029017.

Marchand, R. T., G. G. Mace, and T. P. Ackerman (2008), Hydrometeor detection using CloudSat: An Earth orbiting 94 GHz cloud radar, *J. Atmos. Oceanic Technol.*, 25, 519–533, doi:10.1175/2007JTECHA1006.1.

McGill, M. J., L. Li, W. D. Hart, G. M. Heymsfield, D. L. Hlavka, P. E. Racette, L. Tian, M. A. Vaughan, and D. M. Winker (2004), Combined lidar-radar remotes sensing: Initial results from CRYSTAL-FACE, *J. Geophys. Res.*, 109, D07203, doi:10.1029/2003JD004030.

Naud, C. M., A. Del Genio, G. G. Mace, S. Benson, and E. E. Clothiaux (2007), Impact of dynamics and atmospheric state on cloud vertical overlap, *J. Clim.*, 218, 1758–1770.

Pincus, R., C. Hannay, S. A. Klein, K.-M. Xu, and R. Hemler (2005), Overlap assumptions for assumed probability distribution function cloud schemes in large-scale models, *J. Geophys. Res.*, 110, D15S09, doi:10.1029/2004JD005100.

Potter, G. L., and R. D. Cess (2004), Testing the impact of clouds on the radiation budgets of 19 atmospheric general circulation models, *J. Geophys. Res.*, 109, D02106, doi:10.1029/2003JD004018.

Rossow, W. B., and R. A. Schiffer (1999), Advances in understanding clouds from ISCCP, *Bull. Am. Meteorol. Soc.*, 80, 2261–2288, doi:10.1175/1520-0477(1999)080<2261:AIUCFI>2.0.CO;2.

Rossow, W. B., Y. Zhang, and J. Wang (2005), A statistical model of cloud vertical structure based on reconciling cloud layer amounts inferred from satellites and radiosonde humidity profiles, *J. Clim.*, 18, 3587–3595, doi:10.1175/JCLI3479.1.

Sassen, K. (2002), Cirrus clouds: A modern perspective, in *Cirrus*, edited by D. Lynch et al., pp. 11–40, Oxford Univ. Press, Cambridge, U. K.

Sassen, K., and J. R. Campbell (2001), A midlatitude cirrus cloud climatology from the facility for atmospheric remote sensing: Part I. Macrophysical and synoptic properties, *J. Atmos. Sci.*, 58, 481–496, doi:10.1175/1520-0469(2001)058<0481:AMCCCF>2.0.CO;2.

Soden, B. J., and I. M. Held (2006), An assessment of climate feedbacks in coupled ocean-atmosphere models, *J. Clim.*, 19, 3354–3360, doi:10.1175/JCLI3799.1.

Stephens, G. L., et al. (2002), The Cloudsat mission and the A-Train, *Bull. Am. Meteorol. Soc.*, 83, 1771–1790, doi:10.1175/BAMS-83-12-1771.

Vaughan, M., S. Young, D. Winker, K. Powell, A. Omar, Z. Liu, Y. Hu, and C. Hostetler (2004), Fully automated analysis of space-based lidar data: An overview of the CALIPSO retrieval algorithms and data products, *Proc. SPIE Int. Soc. Opt. Eng.*, 5575, 16–30.

Wang, J., W. B. Rossow, and Y. Zhang (2000), Cloud vertical structure and its variations from a 20-yr global rawinsonde dataset, *J. Clim.*, 13, 3041–3056, doi:10.1175/1520-0442(2000)013<3041:CVSAIV>2.0.CO;2.

Wang, P.-H., P. Minnis, M. P. McCormick, G. S. Kent, and K. M. Skeens (1996), A 6-year climatology of cloud occurrence frequency from Stratospheric Aerosol and Gas Experiment II observations (1985–1990), *J. Geophys. Res.*, 101, 29,407–29,429.

Warren, S. G., C. J. Hahn, J. London, R. M. Chervin, and R. L. Jenne (1986), Global distribution of total cloud cover and cloud type amounts

over land, *Tech. Note TN-273 1 STR*, 29 pp., Natl. Cent. Atmos. Res., Boulder, Colo.

Warren, S. G., C. J. Hahn, J. London, R. M. Chervin, and R. L. Jenne (1988), Global distribution of total cloud cover and cloud type amounts over the ocean, *Tech. Note TN-317 1 STR*, 42 pp., Natl. Cent. Atmos. Res., Boulder, Colo.

Williams, K. D., and G. Tselioudis (2007), GCM intercomparison of global cloud regimes: Present-day evaluation and climate change response, *Clim. Dyn.*, *29*, 231–240, doi:10.1007/s00382-007-0232-2.

Winker, D. M., J. R. Pelon, and M. P. McCormick (2003), The CALIPSO mission: Spaceborne lidar for observation of aerosols and clouds, *Proc. SPIE Int. Soc. Opt. Eng.*, *4893*, 1–11.

Winker, D. M., B. H. Hunt, and M. J. McGill (2007), Initial performance assessment of CALIOP, *Geophys. Res. Lett.*, *34*, L19803, doi:10.1029/2007GL030135.

Wylie, D. P., W. P. Menzel, H. M. Woolf, and K. I. Strabala (1994), Four years of global cirrus cloud statistics using HIRS, *J. Clim.*, *7*, 1972–1986, doi:10.1175/1520-0442(1994)007<1972:FYOGCC>2.0.CO;2.

Zhang, M. H., et al. (2005), Comparing clouds and their seasonal variations in 10 atmospheric general circulation models with satellite measurements, *J. Geophys. Res.*, *110*, D15S02, doi:10.1029/2004JD005021.

_____

G. G. Mace and Q. Zhang, Department of Meteorology, University of Utah, Salt Lake City, UT 84112, USA.

R. Marchand, Joint Institute for the Study of the Atmosphere and Ocean, University of Washington, Seattle, WA 98105, USA.

G. Stephens, Department of Atmospheric Science, Colorado State University, Fort Collins, CO 80523, USA.

C. Trepte, M. Vaughan, and D. Winker, NASA Langley Research Center, Code 435, Hampton, VA 23681, USA.